THE FEBRUARY 9, 1971 SAN FERNANDO EARTHQUAKE: A STUDY OF SOURCE FINITENESS IN TELESEISMIC BODY WAVES

BY CHARLES A. LANGSTON*

ABSTRACT

Teleseismic P, SV, and SH waves recorded by the WWSS and Canadian networks from the 1971 San Fernando, California earthquake ($M_L = 6.6$) are modeled in the time domain to determine detailed features of the source as a prelude to studying the near and local field strong-motion observations. Synthetic seismograms are computed from the model of a propagating finite dislocation line source embedded in layered elastic media. The effects of source geometry and directivity are shown to be important features of the long-period observations. The most dramatic feature of the model is the requirement that the fault, which initially ruptured at a depth of 13 km as determined from pP-P times, continuously propagated toward the free surface, first on a plane dipping 53°NE, then broke over to a 29°NE dipping fault segment. This effect is clearly shown in the azimuthal variation of both long period P- and SH-wave forms. Although attenuation and interference with radiation from the remainder of the fault are possible complications, comparison of long- and short-period P and short-period pP and P waves suggest that rupture was initially bilateral, or, possibly, strongly unilateral downward, propagating to about 15 km depth. The average rupture velocity of 1.8 km/sec is well constrained from the shape of the long-period wave forms. Total seismic moment is 0.86×10^{26} dyne-cm. Implications for near-field modeling are drawn from these results.

INTRODUCTION

It is widely recognized in the seismological and engineering community that the wealth of near- and far-field data obtained from the San Fernando earthquake may represent the single most important data set for understanding the dynamics of a destructive earthquake. Many studies have been made on various aspects of the San Fernando event, each contributing possible constraints on the faulting mechanism depending on which assumptions and which subsets of the data are utilized. For example, near-field strong motion modeling experiments often employ the famous Pacoima Dam accelerograms (Trifunac and Hudson, 1971) and other near-in observations in an effort to deduce source processes (Mikumo, 1973; Boore and Zoback, 1974; Trifunac, 1974; Niazi, 1975; McCowan et al., 1977; among others). Although employing different theoretical representations for source calculations, most of these

---

* Present address: Department of Geosciences, The Pennsylvania State University, University Park, Pennsylvania 16802.

authors make similar important assumptions concerning fault geometry and rupture processes. For example, a common assumption is the interpretation made from the fault-plane solution, hypocentral parameters, and surface ruptures that the fault plane decreases dip with decreasing depth and that rupture proceeded in a unilateral sense from the hypocenter to the surface. Although this is a possible model, the error in hypocentral parameters (Allen et al., 1973) is sufficiently large to admit other fault geometries. For example, it has been suggested by Allen et al. (1973) that the focal mechanism dip of 53°N represents only the very initial motion of the earthquake and that most faulting occurred on a plane dipping about 35°N, as determined by aftershock locations and the initial hypocenter.

Another modeling assumption commonly used is that of uniform slip with uniform rupture velocity along the fault plane. Although relaxed in some studies because of the need to introduce more wave complexity, unknowns such as earth structure and fault geometry are almost certain to introduce significant tradeoffs or ambiguities in interpretations.

A major goal of this paper is to examine these and other assumptions using the teleseismic ($\Delta > 30°$) long- and short-period data set recorded by the WWSS and Canadian networks. Long-period P, SV, and SH waves and short-period P waves will be modeled in the time domain to infer constraints on the geometry of the San Fernando fault and to directly deduce rupture characteristics from a simple fault model. To anticipate major conclusions, it will be shown that the initial hypocenter was at 13 km depth and that rupture was initially bilateral. Because of large short-period P excitation, relative to long-period P, it appears that the initial rupture velocity may have been significantly larger than the average rupture velocity, 3.0 km/sec versus 1.8 km/sec. Fault geometry will be inferred from the observed azimuthal dependence of long-period wave shapes and a fault-plane solution using P and SH first motions. The change in wave shapes requires that the fault plane change dip from 53°N at depth to about 29° at about 5 km.

By placing constraints such as these on the mechanism of faulting for the San Fernando earthquake, it is hoped that future near-field strong motion modeling will yield more fruitful results into the nature of the San Fernando source and into the propagation of its seismic waves in the nearby crust. By demonstrating the utility of the far-field data in determining source processes, it will also become apparent that an approach of combining both the near- and far-field data will yield more unambiguous results than using either alone.

PROCEDURE

All available data for the WWSS and Canadian networks were procured on 70-mm microfilm. Expanded copies 1.8 times larger than the original seismograms were made for digitizing and interpretation purposes. Approximately the first 2 min of the vertical long-period P and all components of long-period S were digitized with an irregular time interval four and two times, respectively. These were averaged to reduce errors due to digitizing and trace line thickness. In addition, a correction for image skew was made to eliminate the inherent distortion of the network's recording systems (Mitchell and Landisman, 1969). Short-period vertical P waves were digitized one time only since trace line thickness was generally small. Some records were high amplitude and faint, however, so that only peaks and troughs were digitized. Long-period records were interpolated to 0.1 sec before averaging to achieve good frequency resolution for deconvolution purposes. Data used in this study are listed by station in Appendix I.

Long-period P wave forms were chosen on the basis of good signal-to-noise ratio (greater than 5) and favorable azimuthal and distance distribution. Wave forms were restricted to lie in the 30° to 90° range to avoid upper-mantle triplications and core shadow effects. S wave forms were rotated into the theoretical back azimuth to obtain radial and tangential displacements. The vertical S wave form was also utilized to determine the onset of prograde elliptical S-coupled P_L particle motion (Helmberger and Engen, 1974).

Analysis of the data was performed in a straightforward manner. Since the free surface is a major influence on the shape of wave forms from shallow earthquakes (Helmberger, 1974) due to the interference of generally large pP and sP phases, estimates of the crustal structure must be included in source models (Langston, 1976a). Synthetic seismograms are calculated for a combined source-structure model using both ray (Langston and Helmberger, 1975) and layer matrix techniques (Haskell, 1953; Harkrider, 1964; Fuchs, 1966; Langston, 1976b). These are then compared directly with observed P and S wave forms to match relative timing and amplitude. This kind of approach has many advantages since a particular pulse or interference effect can be directly interpreted in terms of a particular ray arrival, say pP, or a group of rays. The timing and amplitude is directly related to depth and source geometry in a clear manner. Sources of noise or other complications, for example, S-coupled P_L, can also be isolated and avoided since they can be easily recognized in the time domain as particular arrivals with well defined characteristics.

Two types of source formalisms will be used to describe the body wave radiation from the San Fernando fault. The formalism of an arbitrarily oriented point dislocation given in Langston and Helmberger (1975) will be used only in results from a formal inversion of long-period P wave forms by the methods described by Langston (1976a). Otherwise, this study will investigate radiation from a simple model of faulting, that of a propagating finite line source of dislocation (Hirasawa and Stauder, 1965) embedded in the layered elastic medium. Appendix II describes the nomenclature and conventions assumed for this model. A line segment of dislocation is allowed to rupture bilaterally at a constant rupture velocity from an initial locus of rupture on a rectangular fault plane. The dislocation function at each point on the fault is described by a step or ramp function. The rise time is given as the duration of the ramp. In the far-field approximation, which is assumed here, the dislocation radiation pattern from this finite source becomes independent of its far-field time history. Computational changes from point dislocation theory are therefore minor and only consist of assigning each ray the appropriate down- or up-going P or S wave far-field time function. Depth is referenced to the initial locus of rupture on the fault plane (see Appendix II). Source models of this type have been used by Mikumo (1969) who studied deep and intermediate earthquakes and by Fukao (1971) in a theoretical study of two dislocation sources in a half-space. Although not representing the rupture effect in the width dimension of the fault plane very well, the computational ease the propagating line segment allows more than outweighs its possible shortcomings. This particular model preserves and approximates the overall features of Savage's (1966) fault model which is perhaps a slightly more physical representation. Time functions computed from the two models for similar geometries differ in detail but overall shape and duration are very similar. Convolved through an attenuation and long-period instrument operator the differences become negligible. Final computed ground displacements are either convolved with the 15 to 100 instrument response (Hagiwara, 1958) or the short-period 1.0 to 0.75 response depending on which components are desired. Attenuation is included by convolving displacements with

Futterman's (1962) causal Q operator with constant $t^* = T/Q$ (Carpenter, 1966) where T is the ray travel time and Q the average seismic quality factor along the ray. Values for t^* of 1 and 4 will be assumed for P and S waves, respectively. Uncertainty in Q will be discussed in the modeling results.

LONG-PERIOD WAVE FORM MODELING

Results from the long-period and short-period modeling experiments will be divided since many problems and characteristics involved with the two groups are dissimilar although related through the source model.

In order to obtain meaningful results on rupture processes and propagation effects in body waves as many constraints as possible must be included from previous observations and from internal consistency within the body wave data set. The first important constraint is the location of the initial break. Hanks (1974) suggested on the basis of an S-P (trigger) time taken from the Pacoima Dam accelerograms and tentative identification of pP on short-period teleseismic records that the San Fernando hypocenter was about 5 to 6 km deeper than the P-wave located hypocenter given by Allen et al. (1973), of 8.4 km. A more careful analysis of the same short-period teleseismic recordings confirms Hanks' argument and is given in a later section. The depth obtained here is 13 km from an average pP-P time of 4 sec. I will also adopt his argument for placing the hypocenter about 4 km further north in the region of well located deep aftershocks with thrust mechanisms (Whitcomb et al., 1973). I will also assume that the fault plane intersects the surface at the observed surface breaks and that the Sylmar, Tujunga, and Lakeview fault segments represent the principal extent of thrust faulting (Barrows et al., 1973). This gives a fault width of 10 km. A possibly more stringent assumption is that this width is preserved with depth. Locations of aftershocks given by Whitcomb et al. (1973) suggest that this assumption is generally valid if the aftershocks outline the extent of faulting. I will also suppose that the fault plane is relatively continuous with depth so that no major offsets occur along the dip direction.

The last important constraint is the focal mechanism of the initial break. Focal mechanisms done by various authors (Whitcomb et al., 1973; Dillinger, 1973) are generally consistent and show a well constrained P nodal plane dipping about 50° to 55° north and striking 65° to 70° west of north. The auxillary plane is less well known and can allow from −5° to 25° left lateral motion on the north dipping nodal plane. However, due to a small initial arrival observed in high gain, low noise short-period teleseismic P waves (see short-period modeling section) there exists the possibility that regional first-motion data may be contaminated by a small foreshock. To check this possibility a focal mechanism was determined from what was considered to be the highest quality long-period P and SH wave first-motion data. SH waves were obtained by the vector rotation of the horizontal S wave forms. First motions of SH were determined by looking at the onset of both radial and tangential components and by the smooth azimuthal variation of wave forms between stations. As pointed out by Langston (1976a) and Herrmann (1976) determining the S-wave polarization angle for a shallow source through analysis of the "average" S particle motion is meaningless since the interference of S and sS in SH and S, sS and pS in SV dominates the wave forms. A more rational approach is to either directly model the wave forms (Langston and Butler, 1976) or to simply plot first motions. The latter is not widely used since S nodal surfaces are not simple orthogonal planes as in the P-wave case. Wave form quality was based on high signal-to-noise level and sharp-

ness of the initial break. A simple search and test algorithm was used to determine allowable focal mechanisms for the P and SH data combined. It was hoped that the SH data would help constrain rake and strike since the azimuthal variation of SH for thrust mechanisms is large. The data and results are shown on the focal plots in Figures 1 and 2 and listed in Appendix I. The mechanism was constrained so that an SH nodal surface passed within 5° of KEV, a very distinct direct SH node as seen from the azimuthal variation of SH wave forms. Compressional and shear velocities
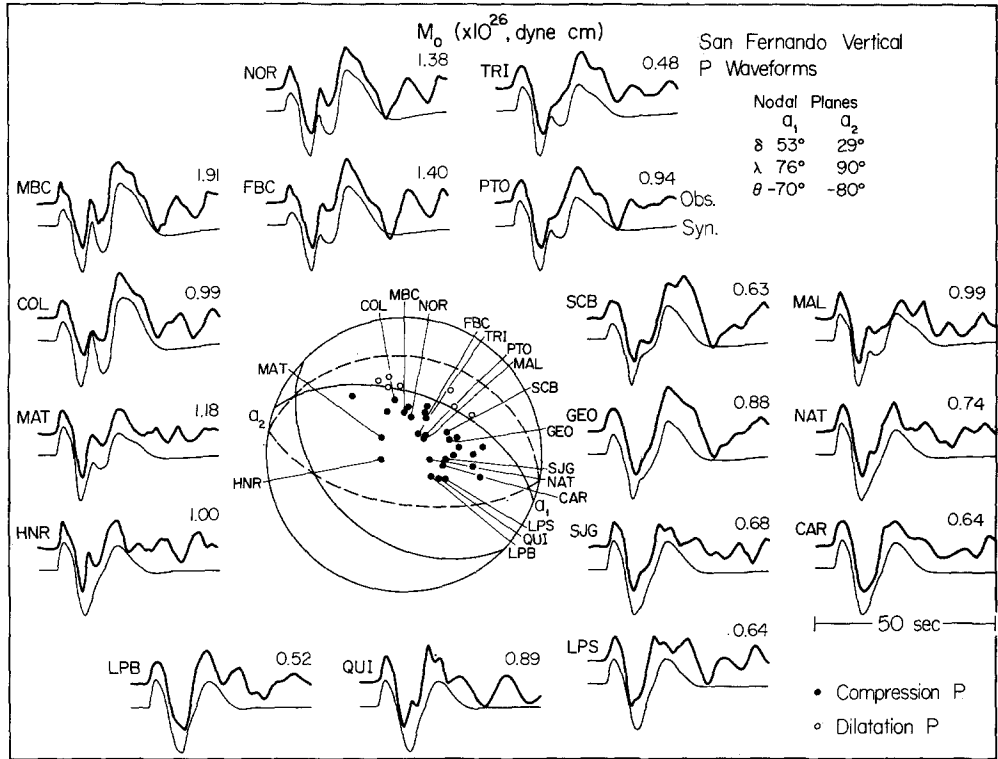

FIG. 1. Observed (*top*) and synthetic (*bottom*) P wave forms at 17 WWSS and Canadian network stations for the final inferred fault model given in Table 5. Each station can be identified by its letter code (see Appendix I). The P first-motion plot is represented by the equal area projection of the lower half of the focal sphere. The nodal planes are for the *bottom* (solid lines) and *top* (dashed lines) sections of the final fault model. The positions of stations used for wave form modeling are indicated by lines to the corresponding P first motion. Many points (compressions) lying near the center were not plotted to improve clarity.

of 6.3 and 3.5 km/sec, respectively, were used for the source medium. The search gave values of dip 53 ± 2°N, rake 76 ± 14° left lateral, and strike −70 ± 8° (W). The uncertainties reflect those solutions which still fit all first-motion data. Throwing out KEV allowed the rake to vary only about 5° more. This solution is not significantly different from previous work and will be adopted for the orientation of the fault in the hypocentral region. It also implies that the small foreshock probably had the same mechanism as the much larger main event.

Details of the crust model used for a particular source orientation can often be important in the final displacement response if S-wave radiation is particularly strong causing significant local S-to-P conversions (Langston, 1976a). However, in dipping dip-slip orientations, P radiation dominates up- and downgoing rays with relatively

minor contributions from S-to-P conversions. Numerical experiments run with thrust sources placed in a multilayered model appropriate for Southern California (Kanamori and Hadley, 1975) gave nearly identical results to that of a simple layer over a half-space with an equivalent velocity contrast at the Moho. Figure 7 demonstrates this
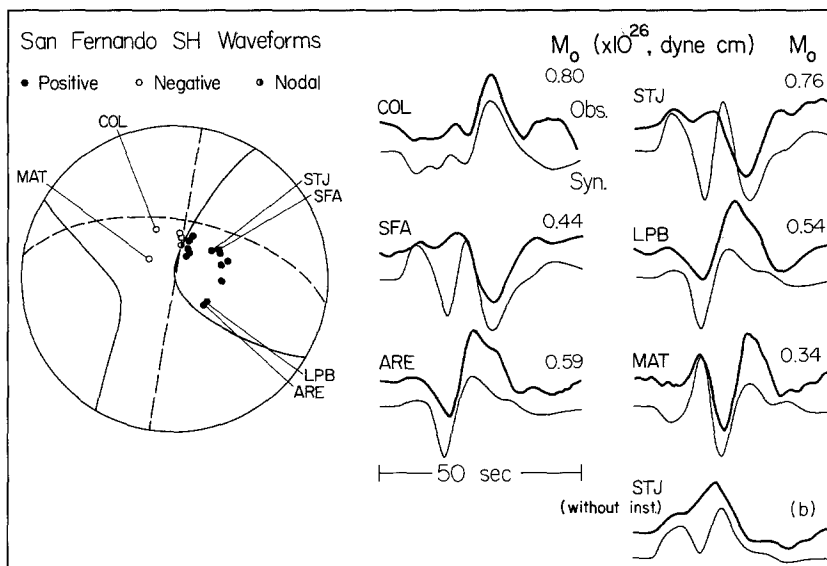

FIG. 2. Observed and synthetic SH wave forms. Same scheme as Figure 1. The wave form labeled (b) is a comparison of the instrumental deconvolution at STJ and synthetic displacement without the instrument.

TABLE 1

CRUST MODELS

Model	α (km/sec)	β (km/sec)	ρ (gm/cc)	Thickness (km)
A	6.0	3.5	2.8	31.0
	7.3	4.2	3.1	—
B	5.5	3.2	2.7	4.0
	6.3	3.6	2.8	23.0
	6.8	3.9	2.9	5.0
	7.8	4.5	3.1	—
C	4.0	2.0	2.6	1.5
	5.5	3.2	2.7	2.5
	6.3	3.6	2.8	23.0
	6.8	3.9	2.9	5.0
	7.8	4.5	3.1	—

for a particular azimuth where sP is relatively strong. Crust model (A) in Table 1 will therefore be used in the finite source modeling because of its simplicity.

Using the constraints of geometry and initial fault orientation we can now investigate different rupture and geometry models for the San Fernando fault. Figure 3 demonstrates the wave shape changes for representative P, SV, and SH wave forms given several geometry models shown in Figure 4. In these models a constant step

dislocation propagates up fault dip at a constant rupture velocity starting at the hypocenter. The sections of the fault which are dipping less than 53° strike N80°W to be more in accord with the surface ruptures and are pure thrust. Small variations
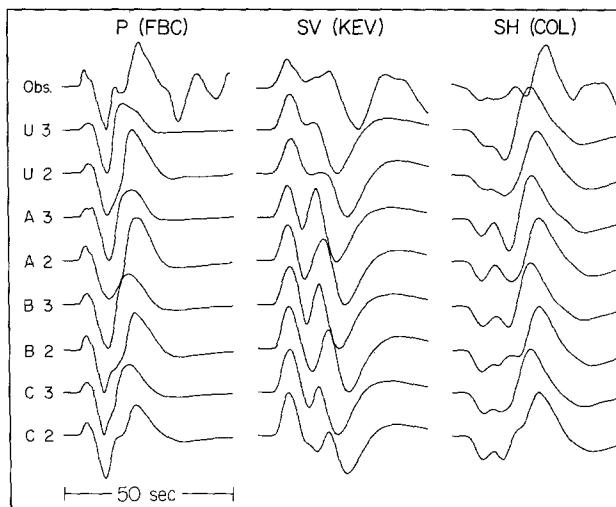

FIG. 3. Comparison of theoretical fault models with representative *P*, *SV*, and *SH* long-period wave forms. The observed is at the top of each column with synthetic wave forms directly below. The first letter of each model represents the fault geometry shown in Figure 4. Geometry U is unilateral rupture from the hypocenter to the free surface on the 53° dippling plane. A, B, C designates fault-plane breakover points at 9, 5, and 3 km, respectively. The values 3 and 2 after each letter indicate the rupture velocity in km/sec.
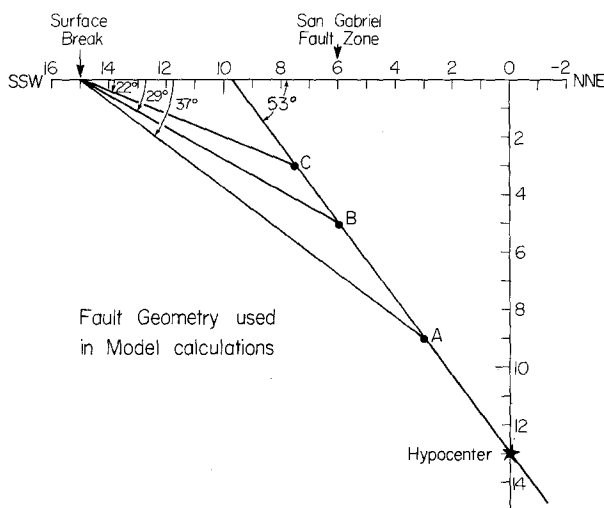

FIG. 4. Fault geometry for the model calculations of Figure 3.

in the strike and rake of these fault segments on the order of the angle variations allowed by the initial rupture do not significantly affect the final wave forms. The principal effects are caused by the timing and duration of rupture and the change in dip. A small fault segment is also allowed to rupture downward away from the hypocenter in models A, B, and C. This proved to be an important effect for modeling

the short-period P waves and will be discussed later. Its effect on long-period wave forms is minor compared to faulting over the upper fault. Model U is a unilateral rupture from the hypocenter to the free surface on the 53° dipping plane. Figure 3 demonstrates the surprisingly good sensitivity that exists for rupture velocity and geometry. Note that in every case where the rupture velocity is 3 km/sec, duration for all wave modes is much too short. The P wave form consists of an initial compressional direct P with a larger dilational downswing about 5 sec later caused by pP. This timing is mainly a function of the source depth. The width of the P wave form, however, appears to increase with decreasing rupture velocity and is caused by the lengthening of the $pP + sP$ interference with direct P. The SV wave forms show an even more striking variation with rupture velocity. The two positive peaks (radial away from source) do not seem to be a very sensitive function of geometry yet their time separation seems to be a nearly direct indication of rupture velocity. These peaks
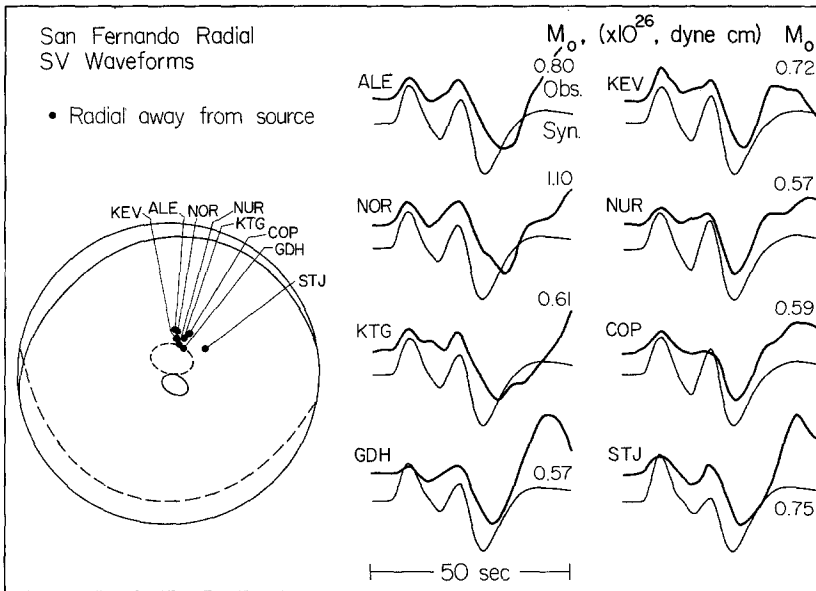

FIG. 5. Observed and synthetic SV wave forms. Same scheme as Figure 1.

are the result of positive direct S and the interference of direct S with positive sS. Note that the second peak increases its amplitude relative to direct S somewhat for models A and B. This is more in accord with the data. The SH wave forms behave similarly to SV, that is, pulse duration increases with decreasing rupture velocity. In this case the change in dip and hence, change in radiation pattern, is more important than in SV. Note the model B2 for SH. The slower rupture velocity combined with the change in dip produced a qualitatively different wave form compared to the other models. Three apparent arrivals are produced from the interference of S and sS from the lower and upper sections of the fault plane. This type of interference is relatively hard to produce on the 15 to 100 system since it requires three consecutive arrivals each larger than the last to compensate for the backswing of the instrument.

Encouraged by these results, it was found that by simply decreasing the overall rupture velocity to 1.8 km/sec and increasing the moment by 20 per cent on the upper fault segment of model B very good fits could be obtained for nearly all P, SV, and SH observed wave forms. Figures 1, 2, and 5 show the observed and synthetic P, SH, and SV wave forms, respectively.

Figure 1 displays 17 P wave form pairs as a function of azimuth. For each pair the observed is on top and synthetic immediately below. The synthetics approximate the shape, timing and duration of first 20 to 25 sec of observed wave forms in nearly all cases. Note the changing interference of the prominent dilational arrival, approximately 10 sec into the record, with azimuth. In northern azimuths this arrival is very prominent. However, the arrival grows smaller going clockwise from north and gradually disappears for southeastern stations. This particular effect comes from the combined interference of direct P, pP, and sP radiated from the 29° dipping section of the fault with those phases radiated from the bottom half. It is interesting to note that the precise timing of this interference was a sensitive function of both rupture velocity and geometry. The model does fail to reproduce some of the details seen in many wave forms. The comparison at HNR is perhaps the worst case. Although the pulse duration is good it is obvious that the observed wave form has experienced greater interference in the reflected phases than predicted.

Arrivals after the first 20 sec may be caused from a combination of effects. Aftershocks were numerous and, in particular, there was an unlocated $M_L = 5.8$ event about 30 sec after the main event (Hileman *et al.*, 1975). This is of reasonable size and could conceivably explain the consistent arrivals seen 25 sec into the P wave forms. Unmodeled earth structure may also contribute to the coda, although this is unlikely for simple layered structures and these fault orientations.

Figure 2 displays the few good SH observations with synthetics. These SH wave forms were chosen from the many S-wave rotations on the basis of good signal-to-noise ratio and being of comparable amplitude to direct SV. The visual fit is, in general, less good than the P waves. It was found that by varying the rake and strike angles of the upper fault plane some improvement could be made for the stations STJ and SFA but to the detriment of the P wave form fits. The comparison for the other SH wave forms changed little when this was done. However, part of the difficulty in fitting SFA and STJ lies in the fact that instrument interference is very large due to the timing of the SH displacement. Comparison of the observed displacements without the instrument (Figure 2b) reveals two positive peaks about 10 sec apart, the first of which is half as large as the second. The synthetic displacement, however, fits the peak timing but not the precise amplitude or shape. It is felt that even this quality of fit is a significant indicator of the change in dip of the fault plane since it was not possible to produce synthetic displacements with the prominent double peak without the substantial dip change. The general aspect of these SH wave forms, like the P wave forms, is one of interference. Direct S is only apparent in the first few seconds and is even sometimes nodal (LPB, ARE). The remaining part of the wave forms are dominated by sS from the bottom fault segment interfering with S and sS from the top section. These phases all arrive within several seconds of each other and each with effective time functions about 6 or 7 sec in duration.

The SH moments also seem to scatter more and are lower, in general, than the P waves (Figure 1). These moments were computed by taking the amplitude of the first peak for COL, STJ, and SFA, and the second for LPB, ARE, and MAT. The P moment was computed from the amplitude of direct P which is relatively uncontaminated by pP. The reasons for the amplitude and shape problems in the SH wave forms and missing interference details in the P wave forms may lie in the fact that most geological evidence indicates that the hanging wall of the San Fernando fault may be resting on an extremely thick Miocene and Plio-Pleistocene sediment section (Johnson and Duke, 1973). Deep drill holes and velocity measurements immediately to the south of the fault ruptures indicate that sediments may be as thick as 4 or 5 km

(Duke *et al.*, 1973). If so, then the entire 29° dipping segment of fault model B would also form a substantial velocity discontinuity. Although the precise effect this would have on teleseismic radiation is at present unknown, studies of dislocation sources in slightly dipping media indicate that wave form distortion could be significant (Langston, 1977). The effects of dipping interfaces were found to be largest for those sources which amplified the small ray azimuth anomalies through radiation patterns which varied fast with azimuth. By analogy, *SH* radiation will be more strongly affected by the fault structure than will the *P* radiation since the *SH* radiation pattern changes much more quickly with azimuth than does *P* (see Figures 1 and 2). A further complication may be the left-lateral strike-slip "Chatsworth segment" (Whitcomb *et al.*, 1973) inferred from aftershock locations and focal mechanisms. This particular fault may have ruptured during the main event and could conceivably complicate the radiation of the upper thrust segment. Because of the potential problems of a dipping velocity discontinuity, however, no attempt was made to include this possible source feature.

Synthetic and observed radial *SV* wave forms are displayed in Figure 5 along with theoretical radiation patterns from the lower and upper fault sections. In using these wave forms care was taken in recognizing the potential problems that shear-coupled *PL* and local receiver structure could present in their interpretation. Radial *SV* wave forms were used instead of the vertical component to minimize contributions from *SP* and other crustal reverberations (for example, see Burdick and Langston, 1977). Wave forms for stations at distances less than 45° were not used because of the theoretical phase shift introduced by the complex transmission coefficient at a typical Moho velocity discontinuity. Furthermore, reverberations and *S*-coupled *PL* waves are much larger inside this range since *P* energy is easily trapped in the crustal wave guide (Oliver, 1961; Gilbert, 1964; Su and Dorman, 1965) due to the *P* critical angle at the Moho. Observationally, *S*-coupled *PL* waves are often seen at ranges past 45° as well. Examination of the vertical-radial particle motion for the wave forms of Figure 5 showed that significant vertical motion only arrives after the first two positive peaks and starts in the large negative backswing. Because of these reasons and the combination of good signal-to-noise ratio and good consistency among wave forms in this relatively small azimuth range, the first 20 to 25 sec of *SV* record are believed to be a good representation of *SV* radiation and interaction in the source area. These wave forms are relatively insensitive to details in the orientation of the fault as can be seen in the radiation patterns of Figure 5 and in the model study of Figure 3. Their principal redeeming characteristic is their sensitivity to rupture velocity. The separation of the two peaks plus the interference of radiation from the lower and upper fault segments in the *P* waves gives a value for rupture velocity of 1.8 km/sec. As in the case of many of the *SH* waves discrepancies in the shapes of these *SV* wave forms are exaggerated by the instrument response. The second pulse is generally about two or three times the amplitude of the first as seen without the instrument. In many respects, however, this instability is advantageous since it gives greater resolution to the modeling process.

The average moment for the 17 *P* wave forms of Figure 1 is $0.93 \pm 0.37 \times 10^{26}$ dyne-cm; that for *SV* is $0.73 \pm 0.18 \times 10^{26}$ dyne-cm. The *SV* moment was computed using the amplitude of the first arrival and scaling the synthetics appropriately. The difference in moment is not significant considering the standard error of each wave form set. The average moment combining the *P* and *SV* wave forms is $0.86 \pm 0.33 \times 10^{26}$ dyne-cm. The *SH* wave form data is not included in the average because of

its irregularity and potential structural problems. Receiver structure assumed for these amplitude measurements is a simple half-space with compressional and shear velocities of 6.0 and 3.5 km/sec, respectively. Lowering these velocities to 5.5 and 3.2 km/sec would decrease the average moment by 10 per cent, or to 0.77×10^{26} dyne-cm.

The approximate structure of the fault plane is also suggested by formal inversion results involving point dislocation models for the P wave forms. Through extensive trial and error variation of point dislocation parameters (Langston, 1975) a two-point source starting model was deduced to fit the observed P wave forms of Figure 1. The

TABLE 2

INVERSION RESULTS

Parameter*	Iteration					
	Starting Model	1	2	3	4	5
$\delta_1 (^{\circ})$	45.0	43.5	45.8	42.4	44.1	43.0
$\lambda_1 (^{\circ})$	70.0	75.6	83.1	77.3	79.6	77.3
$\theta_1 (^{\circ})$	−70.0	−69.9	−67.6	−72.2	−79.1	−77.9
h_1 (km)	14.0	15.1	15.1	14.9	15.1	15.2
δt_{11} (sec)	0.01	0.28	0.89	0.54	0.35	0.39
δt_{21}	3.50	2.97	2.60	2.58	2.71	2.60
δt_{31}	1.00	0.77	0.78	1.32	1.59	1.64
δ_2	40.0	28.1	24.0	18.9	17.9	18.9
λ_2	85.0	84.2	92.8	92.2	95.7	95.1
θ_2	−80.0	−80.2	−84.8	−77.3	−79.6	−78.5
Mo_2	0.64	0.65	0.70	0.64	0.60	0.59
$TLAG_2$ (sec)	6.0	5.55	5.19	4.85	4.95	4.94
X_2 (km)	−8.0	−7.8	−8.7	−9.3	−9.5	−9.7
Y_2 (km)	0.0	−0.5	−0.5	−2.0	−2.1	−2.2
h_2	6.0	6.6	8.3	9.1	9.8	10.7
δt_{12}	0.01	0.01	0.40	1.10	1.15	1.17
δt_{22}	3.50	4.21	4.42	3.42	3.14	3.14
δt_{32}	0.01	0.01	0.01	0.10	0.01	0.01
ϕ average	0.9508	0.9566	0.9594	0.9620	0.9628	0.9616

* From Langston, 1976a: δ_i (dip of ith source), λ_i (rake), θ_i (strike clockwise from north), h_i (depth), $TLAG_i$ (time lag), X_2 (horizontal distance from first source, north positive), Y_2 (east positive), $\delta t_{1i}, \delta t_{2i}, \delta t_{3i}$ (time duration of the positive, zero and negative slopes, respectively, of a trapezoid time function.)

parameters for this model are displayed in Table 2. The inversion procedure is outlined in Langston (1976a) using ideas presented by Mellman *et al.* (1975). A two-layer crust model similar to model B, Table 1, served as the local source earth structure. In arriving at this particular starting model no outside constraints were used as in the finite fault modeling. The shapes of the P wave forms were the only basis in determining the model. Figure 6 displays a comparison of the observed with the inversion result after five iterations. Table 2 shows the variation of parameters with each iteration. The average value of ϕ, the correlation function, indicates the quality of fit. A value of unity for ϕ means a perfect match in wave forms. Because the number of parameters (18) was larger than data (17) and because an eigenvalue cutoff based on the variance of the parameter changes was used, the inverse problem was under-determined. In general, about 10 out of 17 eigenvalues were retained for each iteration. Examination of the parameter resolution matrix suggested that δ_1, δ_2, Mo_2,

δt_{11}, $TLAG_2$, h_1, and h_2 were the more important parameters in the inversions. This agreed very well with the intuition and experience acquired from the trial and error wave form fitting. A comparison of Figures 1 and 6 indicates that the two fault models, although conceptually different, give strikingly similar fits. In fact, the average correlation function for the finite fault model is nearly identical (0.96) to that of the point source model. The major discrepancy in the point source model, aside from some orientation differences, is the depth of the upper source. Otherwise, some general
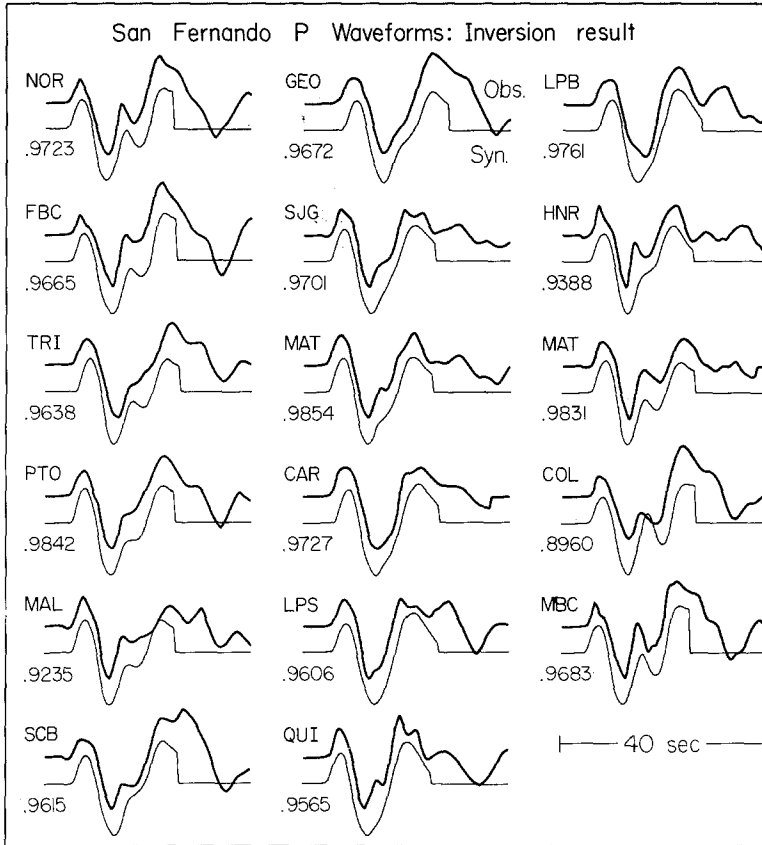

FIG. 6. Observed (*top*) and synthetic (*bottom*) P wave forms at the same 17 stations of Figure 1. Fault model is the two-point source inversion result of Table 2. The number by each wave form pair is the value of the correlation function indicating the quality of fit.

characteristics of the finite model are preserved. There is a distinct change in fault dip from about 45° to 19° and the apparent rupture velocity between sources is approximately 2.2 km/sec as determined by their spacing and time lags. The simple two-point source model did not predict the observed SV or SH wave forms, however. Inclusion of the finite fault model with vertical directivity was done for this reason. It was found that although upgoing and downgoing long-period P-wave time functions were not very sensitive to geometry and rupture velocity shear wave time functions were strongly affected. Only when direct S was longer in duration and smaller amplitude than the surface reflections could the SV and SH interference be adequately modeled. The point source P model results do suggest, however, that even where vertical directivity is an important factor for dipping dip-slip orientation, teleseismic

P waves can be interpreted with point source theory to meaningfully test for possible source complications.

SHORT-PERIOD WAVE FORM MODELING

Inclusion of the short-period P-wave teleseismic data set with the long-period wave form modeling provided a good constraint on source depth and further interesting insights into the nature of body wave radiation from the San Fernando earthquake. Figure 7 shows what one might expect the vertical short-period P wave form to look like for a typical thrust point source embedded in various layered earth models (Table 1). The time function is very short so that the shape of each phase shown under "displacement" is mainly that of the Q operator. These seismograms were computed using the layer matrix formulation so that all multiples are included. Both the displacements and displacements convolved with the short-period instrument response
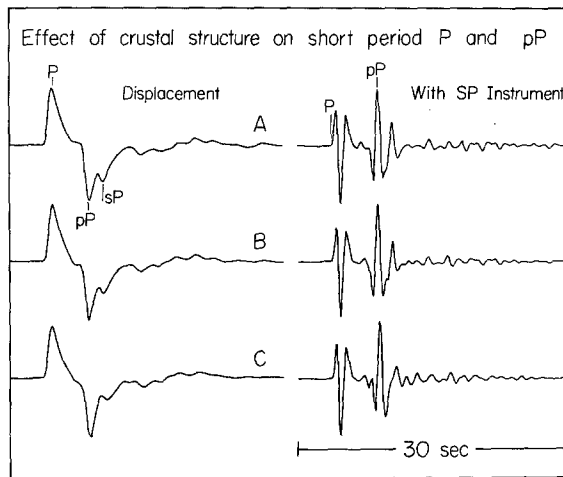

FIG. 7. Effect of crustal structure on short-period P, pP, and sP for a typical thrust fault orientation. The displacements without (*left*) and with (*right*) the short-period instrument are computed for the indicated crust models of Table 1 using the layer matrix formulation. Source depth is 13 km, dip 48° (NE), rake 78°, and strike −66° (NW). Station azimuth is 24.2° and distance 77°. The time function for the point source is an isosceles triangle 0.5 sec in duration.

demonstrate that compressional P and dilatational pP are the predominant phases. The phase sP is generally half the amplitude of pP although it can be comparable for certain ranges of distance and azimuth. Furthermore, the amplitude ratios of P and pP change very little with changing structure although sP may be reduced significantly by low-surface velocities. These seismograms also demonstrate that the theoretical effect of crustal multiples, seen as the small oscillations after sP, is minor.

For a simple impulsive source these large phases should then be obvious. The question is whether the short-period data will yield this information. The long-period wave form study showed that faulting was relatively continuous for at least 10 sec, hardly an impulsive source in the short-period band. Figure 8 shows the results of several stacking experiments in an effort to find the phase pP while reducing the effect of noise and station structure. Several criteria were applied in choosing the short-period P wave forms for both stacking and modeling. Wave forms were rejected if their coda amplitude was comparable to the short-period direct wave in the region where the long-period coda was small. Short-period wave forms were also suspect if the hori-

zontal components were of higher relative amplitude at long durations (~30 sec) and if the wave shapes and relative amplitudes of the first few seconds were dissimilar between components. This last observation probably implies dipping or other non-horizontal station structure (Langston, 1977). In the left column of Figure 8 are averages of the short-period P time series distributed by groups. Seismograms were grouped together for those stations within the approximate limits of 30° azimuth and distance sectors. The seismograms were then normalized to the maximum amplitude of the first 5 sec and averaged. The moveout for pP relative to P is at most 0.3 sec between 30° and 80° for a 13 km source, and so, can be neglected. The theoretical amplitude of pP relative to P based on the focal mechanism also changes very little in the range of
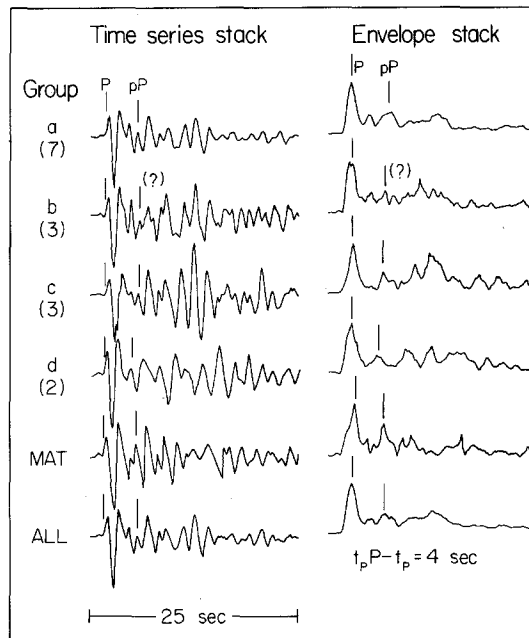

FIG. 8. Time series (*left*) and envelope (*right*) stacks of short-period vertical P wave forms Stations for each group are listed in Appendix I. Arrows indicate P and pP picks. The traces labeled "all" are the average stacks of all 16 short-period stations used above.

each azimuth sector. In fact, part of the basis for deciding on these particular ranges was the similarity of wave forms between stations. Using the approximate focal depth of 15 km determined by the inversion results and the wave shape and polarity information of Figure 7, a dilational pP pulse can be expected 4 to 5 sec after the direct P. Indeed, such a pulse can be generally observed in the time series stacks and is indicated by the arrows. The average time difference between pP and P is 4 sec, corresponding to a depth of 13 km. This substantiates Hanks' (1974) tentative identification of this phase. The same result can be found by examining the average of the normalized instantaneous amplitude of the analytic signal (Farnbach, 1975; Langston and Blum, 1977) shown on the right side of Figure 8. The area of the first 4.5 sec corresponding to the first large peak was normalized to unity for each seismogram envelope.

Stacking each group these two independent ways demonstrates that the relatively small amplitude for pP seen in the time series is not an artifact of interference re-

sulting from the averaging procedure. The complex envelope is a slowly varying function of time, relative to its corresponding time series, so that small time shift errors will not affect the average. This small pP amplitude, relative to P, represents an anomaly since the radiation pattern from the long-period focal mechanism requires pP to generally be the same size or larger than direct P. It has also been shown, however, that vertical directivity is important in the long-period waves so that the discrepancy may be explained by source propagation effects.
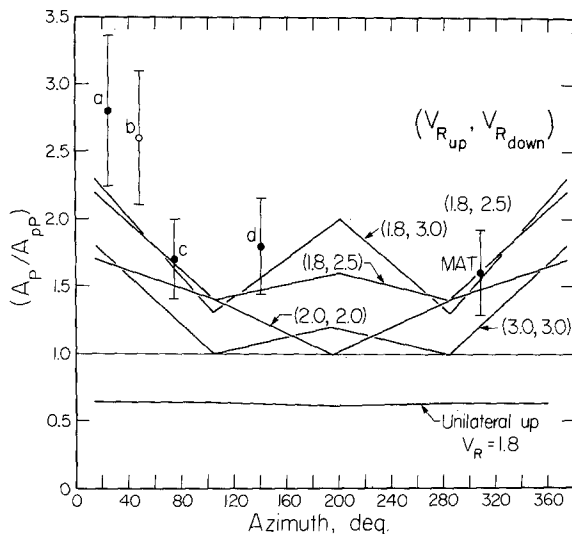

Fig. 9. Points are the corrected amplitude ratio of short-period P to pP for the stack groups of Figure 8 versus azimuth. Error bars correspond to 20% error in amplitude measurements. Amplitude ratio has been corrected for radiation pattern and free surface reflection coefficient (Table 3). Lines indicate various theoretical rupture models.

TABLE 3

SHORT PERIOD A_P/A_PP RATIOS, OBSERVED AND CORRECTED

Stack Group	Number	Δ (°) (average)	AZ (°) (average)	A_P/A_PP	
				Observed	Corrected
a	7	71.5	23.7	2.5	2.8
b	3	57.3	47.9	2.5	2.6
c	3	31.3	73.9	2.2	1.7
d	2	62.3	139.1	2.5	1.8
MAT	1	79.7	307.2	1.7	1.6

Figure 9 condenses the results of several short-period modeling experiments. In this figure the amplitude ratio of short-period P, A_P to short-period pP, A_PP, corrected for radiation pattern and free surface reflection coefficient for model A, Table 1, is plotted versus azimuth. Table 3 lists the observed amplitude ratio for each stacking group with the corresponding corrected value. Amplitudes for P and pP were taken from the maxima of the P and pP peaks designated on the envelope stacks. A simple comparison of envelope and time series stacks shows that these amplitudes correspond to the maximum amplitudes for each pulse. The curves on Figure 9 correspond to several different rupture and fault geometry models. The line $A_P/A_PP = 1$ is the expected value for this ratio if there are no source propagation effects. In the

remaining models, rupture is allowed to propagate only up to the 29° dipping fault segment of model B, Figure 4, and no further. As will be shown, nearly all of the important short-period information occurs at the very initiation of rupture. The simple unilateral model with a rupture velocity of 1.8 km/sec, appropriate for the long-period wave forms, fails to even approximate the observed amplitude ratios. In this model, pP is considerably larger than P. However, simply by making the fault initially bilateral, corrected pP starts becoming smaller than P. All of these rupture models assume a step dislocation time history and are computed for a distance of 50° at azimuths of 0°, 90°, and 270° from the end of the 53° dipping fault plane. Symmetry relations are used to get the model values at 180° (0°) since rupture is constrained to propagate up or down dip only. It was found that a small 2 km extension of the fault
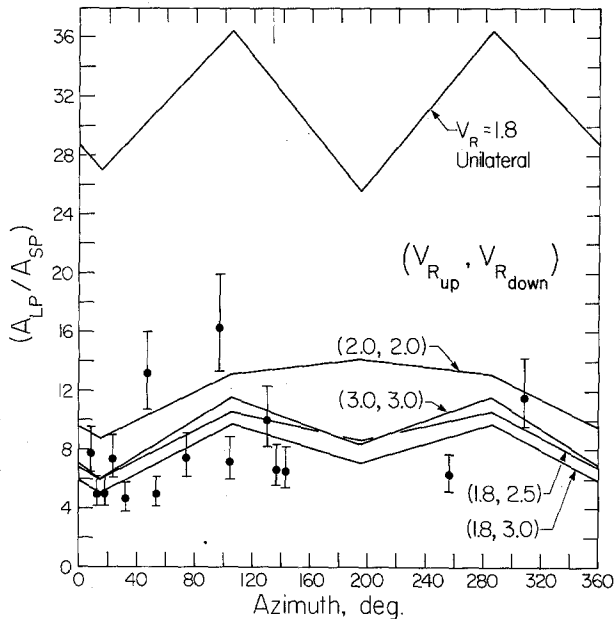

FIG. 10. Points are the amplitude ratio of long-period P, A_{LP}, versus short-period P, A_{SP}, plotted versus azimuth (Table 4). Error bars represent 20 per cent measurement errors in both amplitudes. Lines indicate various theoretical rupture models.

below the hypocenter (see Figure 4) could satisfactorily explain the duration and shape of short-period direct P. Note, however, that pulse duration is mainly controlled, to first order, by the ratio (L/V_R), where L is the fault length (see equation A5, Appendix II). Without other constraints, therefore, length can trade off directly with rupture velocity. Keeping the fault length of the small section constant, it was found that even by assuming relatively high rupture velocity the observed amplitude ratios could not be fit by a simple bilateral arrangement. However, if the rupture was made effectively unilateral, propagating downward, then the observed and calculated approached each other. This was done, somewhat arbitrarily, by simply assigning a faster rupture velocity for the small fault segment, keeping the rupture velocity on the upper segment at 1.8 km/sec to be consistent with the long-period result.

Further constraints on these models comes from long-period P, A_{LP}, to short-period P, A_{SP}, amplitude ratios shown in Figure 10. Data for this figure are tabulated in Table 4. Amplitude measurements for direct long-period P are taken from the first positive arrival (see Figure 1). The short-period amplitude measurement is, again,

the maximum of the direct P pulse. Theoretical models shown on Figure 10 are those of Figure 9. The principal result of this study is that the upward propagating unilateral fault model totally fails to provide sufficient short-period excitation. The various bilateral fault models group together for the most part and are generally consistent with the data. If any model was to be chosen as the "best" model from Figures 9 and 10, probably the (1.8, 3.0) model would be appropriate. Unfortunately, however, there is a strong tradeoff of A_{LP}/A_{SP} with Q. If a t^* of 0.7 is assumed instead of 1.0, theoretical amplitude ratios decrease by nearly a factor of 2. A_P/A_PP also tends to decrease. This can be compensated for, in turn, by increasing the dislocation rise time. This also affects the rupture velocity estimates for the lower fault segment through L/V_R. Increasing t^* would necessitate models of larger dislocations on the

TABLE 4

OBSERVED $A_{LP}/A_{SP}P$ AMPLITUDE RATIOS

Station	Δ (°)	AZ (°)	A_{LP}/A_{SP}
ALE	51.8	8.0	7.96
KEV	73.1	11.9	5.05
NUR	80.7	17.5	4.99
KTG	60.1	22.7	7.40
FBC	42.2	30.5	4.76
PTO	81.0	46.0	13.25
STJ	49.9	53.8	4.99
BLA	30.8	73.7	7.58
NAT	87.2	98.5	16.30
CAR	52.5	104.2	7.23
ARE	67.4	130.6	10.11
GIE	43.8	137.1	6.79
PEL	80.7	141.0	6.72
HNR	88.5	257.6	6.33
MAT	79.7	307.2	11.69
Average			8.08
σ			3.37

bottom segment relative to the rest of the fault. Nevertheless, these models clearly show that the unilateral upward fault model is unacceptable.

Synthetic seismograms were computed for three of the best short-period observations in which the phases P and pP could be clearly distinguished. This was done to check the consistency of the depth estimate and amplitude measurements. A rationale of picking the cleanest recordings was used in order to avoid interference from possible unmodeled arrivals, such as those between P and pP in groups (a) and (b), Figure 8. Figure 11 displays the observed and synthetics. The final fault model is given in Table 5. It incorporates the long-period wave form results with the (1.8, 3.0) model of Figures 9 and 10. These synthetics demonstrate that the timing, shape, and relative amplitude of P and pP are well represented by this simple fault model, although there are some obvious problems with sP at ATL. This may only be an artifact of the simple layer over half-space model. As seen from Figure 7, low-velocity material near the surface can reduce sP by up to 50 per cent in amplitude. Shown below the synthetics are the time functions for P and pP from the 53° dipping fault segment. In each case, the sharp spike at the beginning of the pulse is due to the downward propagating fault segment plus the response of a small part of the upward propagating fault

segment. This characteristic is the reason the short-period observations are relatively clean and also high amplitude. The bilateral rupture model for the hypocenter has important implications for near-field strong motions. It implies that previous unilateral fault models may be overestimating slip in the hypocentral region by a factor
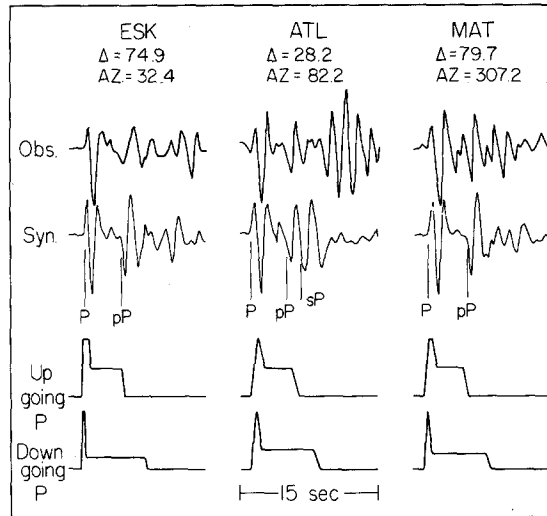

FIG. 11. Observed (*top*) and synthetic (*directly below*) short-period vertical P wave forms for three select stations. Model is final model of Table 5. Theoretical P-wave time functions from the bottom section of the final fault model are shown for upgoing and downgoing rays appropriate for each station.

TABLE 5

FINAL INFERRED SAN FERNANDO FAULT MODEL
(*Model is based on geometry B, Figure 4*)

	Lower Segment	Upper Segment
Depth (km)	13	5
Strike (°)	−70	−80
Dip (°)	53	29
Rake (°)	76	90
Fault width (km)	10	10
Fault length, up-dip (km)	10	10.5
Fault length, down-dip (km)	2	—
Rupture velocity, up-dip (km/sec)	1.8	1.8
Rupture velocity, down-dip (km/sec)	3.0	—
Rise time (sec)	0	0
Moment (dyne-cm)	0.41	0.45

Average slip (both segments) = 1.1 meters

of 2 since inclusion of the small fault segment below the hypocenter effectively doubles the far-field displacement in the first second or so. This would help explain the sharp initial S velocity pulse seen at Pacoima Dam (Hanks, 1974; Boore and Zoback, 1974) without resorting to high initial dislocations.

The observed at ATL shows a distinctive series of large amplitude arrivals several seconds after pP. These arrivals are also clearly shown in the stacks of Figure 8, being largest for group (c) but also apparent in groups (a) and (b). Figure 12 shows a com-

parison of long-period P and short-period P at two stations with theoretical arrival times of major phases for the fault model indicated by dashed lines. FBC is in a similar azimuth to ESK but is 23° closer in distance. A theoretical wave form for FBC would be very similar to ESK, however, and would not show any major arrivals after pP besides sP. Hanks (1974) suggests these arrivals signify the so-called "breakout phase", i.e., radiation associated with the rupture of the earth's surface. Indeed, the timing is appropriate for a source at the surface, but since several other phases are required at this arrival time this particular interpretation is interesting but can only be conjecture at best. No attempt was made to model these arrivals since they are probably associated with the upper fault segment. They may represent "roughness" on the dislocation time function, other sources, or effects due to the possible velocity contrast across the fault surface.
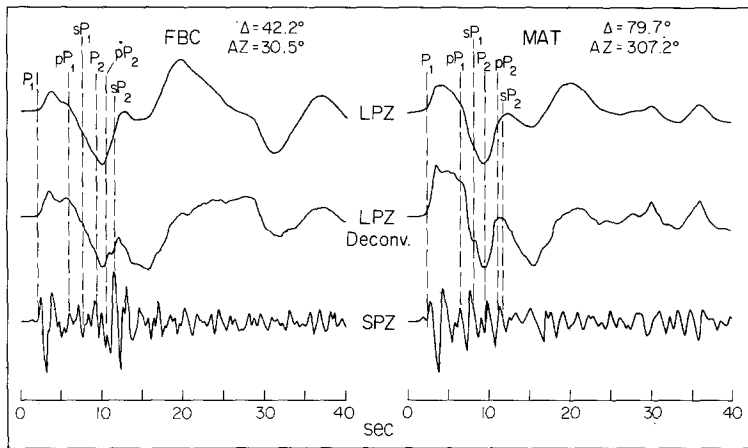

FIG. 12. Comparison of long-period vertical, long-period vertical instrumental deconvolution, and short-period vertical P wave forms at two stations. Dashed lines indicate theoretical arrival times for the major phases of the final model, Table 5. The subscripts 1 and 2 indicate radiation from the lower and upper fault segments of the final model, respectively.

Figure 12 clearly demonstrates the interference of the major theoretical arrivals from both sections of the fault. Six large phases of unequal amplitude and different polarity all arrive within a span of 10 sec. Note also the sharp initial peak in the long-period instrument deconvolutions for direct P_1. Although attenuation is still included, the shapes are consistent with the time functions of Figure 11. The short-period observations of Figure 12 show a small positive arrival about 0.5 sec before impulsive direct P. This was a commonly observed arrival for those observations which were high gain and low noise. It is interpreted to be either a small foreshock or roughness in the dislocation function for the main event; the difference maybe being semantic.

DISCUSSION

Several questions involving the parameterization have yet to be addressed. One concerns the effect of dislocation rise time. The long-period S wave forms can accept up to several seconds of rise time without significantly affecting the rupture velocity estimate. Wave interference for the SV wave forms was primarily due to the changing depth of the fault plane with time. Interference in the long-period P wave forms would tend to smooth with increasing rise time, however. Furthermore, the short-period wave shapes require an initial high amplitude pulse of about 1 sec in duration. If the

rupture velocity was at compressional velocity, the limiting case, at most only about 1 to 2 sec of rise time would be permitted, depending on reasonable estimates of Q. This can be taken as an upper limit for the initial fault break.

The increase in moment for the upper fault segment can be due to several effects. These may involve slightly changing fault width with depth, different velocity distribution other than the simple layer model assumed, or possible variation in dislocation along the fault. Either or all of these effects may be important and would trade off with each other in predictable ways. To obtain better estimates for these kinds of variations, fault geometry and earth structure must be known to higher precision.

Table 6 lists moment determinations for the San Fernando earthquake done by various authors and with different techniques. All values are generally consistent within a factor of 2 and average to about 1.0×10^{26} dyne-cm. In detail, however, there may be an indication of bias in the body wave results relative to the surface wave and static displacement results of Alewine (1974). Alewine's surface wave study incorporated 18 azimuthally distributed observations of the fundamental Rayleigh wave

TABLE 6
MOMENT DETERMINATIONS

Source	Data	Mo ($\times 10^{26}$ dyne-cm)
Canitez and Toksöz (1972)	Surface waves	0.75
Canitez and Toksöz (1972)	Static (3D)	1.64
Wyss and Hanks (1972)	Teleseismic P waves	0.47
	Teleseismic S waves	0.88
Mikumo (1973)	Static (3D) and near-field	1.1
Jungels and Frazier (1973)	Static (2D)	0.62
Trifunac (1974)	Near-field	1.53
Alewine (1974)	Surface waves	1.7
Alewine (1974)	Static (3D)	1.0–2.2
McCowan et al. (1977)	Static (2D)	0.4
This study	Teleseismic P and SV waves	0.86 ± 0.33

periods up to 60 sec and assumed a fault model similar to that deduced in this study. As such, Alewine's results are probably more reliable than those from Canitez and Toksoz (1972) who employed fewer stations and a significantly different fault orientation model. Alewine's surface wave moment is 1.7×10^{26} dyne-cm compared to 0.86×10^{26} dyne-cm obtained from the body waves. The factor of 2 difference may be significant and may reflect actual differences in excitation of the seismic spectrum at the long- and short-period ends as suggested by Hart et al. (1977) for the Oroville earthquake. Some possibilities include slow fault slip after initial high slip rates or slow extension of the fault plane in the down dip direction from the initial hypocenter. This last possibility is interesting since it has been shown that, at least initially, the fault rupture was bilateral and with possible initial high rupture velocity implying high effective stress relative to the rest of the fault. Intuitively, it seems unlikely for such energetic rupture to suddenly stop at depth without extending itself in some manner although mechanisms can be constructed which do so. It may be, for example, that preseismic creep along the downward extension of the San Fernando fault actually relieved stresses at depths greater than 15 km while producing a stress concentration near the eventual hypocenter of the earthquake, the top edge of the creeping zone. Rupture would then stop upon encountering the relatively stress-free region below the fault. This last idea is motivated by recent geodetic interpretations made by Thatcher (1976) for the San Fernando region.

The moment difference may also be a result of unknown wave propagation factors for either the body or surface wave studies. One relatively unknown parameter for body waves is attenuation. A check on the consistency of the Q model was done using observed long-period and short-period S-wave amplitudes (Burdick, 1977). A search for observable short-period S waves turned up only one usable wave form and at the station NOR. Usually, the short-period signal was unobservable by apparently being well into the noise, a very significant observation in itself. The short-period components at NOR, however, were run at a magnification of 50,000 rather than the usual gain of 25,000 as at most other stations. Combined with very low noise, the EW component yielded a short-period SV wave 0.033 microns in amplitude. The long-period/short-period amplitude ratio for direct SV was 290 ± 120. Because the source model was a very efficient radiator of short-period P, short-period S should be comparable if there is no attenuation effect. A theoretical calculation using the final source model of Table 5 for $t^* = 4.0$ gave an amplitude ratio of about 200, consistent with the observations and modeling assumptions, assuming no energy loss in compression (Anderson et al., 1965). In any case, an interpretation of this possible moment anomaly should wait until further relationships between the seismic data, especially in near-field/far-field body waves, are worked out.

Errors induced in the model from the long-period/short-period amplitude ratios for direct P and S are principally due to unknowns in attenuation and, possibly, geometrical spreading. Because the data are relatively consistent over a wide distance range (Figure 10 and Table 4) unknowns in short-period geometrical spreading are probably not important. Errors in this amplitude ratio were investigated for differing receiver structures but it was found that only a 10% change in A_{LP}/A_{SP} could be obtained from widely different elastic structures. These ranged from a simple half-space to a structure with very low-surface velocities corresponding to a thick sedimentary section similar to model C, Table 1.

Variation in attenuation is not a large factor for the short-period pP and P amplitude ratio. Radiation pattern is very well known and changes little with azimuth. The nature of the free surface reflection coefficient may be a problem, however. Although I have shown that A_P/A_PP changes little with simple layered structures (Figure 7), surface topography has not been considered. Including this effect would allow the reflection coefficient to become a function of frequency. To determine the magnitude of this effect the results of Sato (1955) will be used. For a normally incident plane P wave on a sinusoidally corrugated free surface on a half-space, the reflection coefficient, A_0, is given by

$$A_0 = -1 + \frac{\alpha^4}{\beta^4} \frac{k_\alpha{}^5 (k^2 - P^2)^{1/2} c^2}{\left(\dfrac{\alpha^2}{\beta^2} k_\alpha{}^2 - 2P^2\right)^2 + 4P^2 (k_\alpha{}^2 - P^2)^{1/2} (k_\beta{}^2 - P^2)^{1/2}} \tag{1}$$

where

$$\omega = \text{angular frequency}$$

$$k_v = \omega/v$$

$$\alpha = \text{compressional velocity}$$

$$\beta = \text{shear velocity}$$

and where topography on the free surface is described by the equation

$$z = c \cos Px,$$ (2)

so that

c = amplitude of corrugation

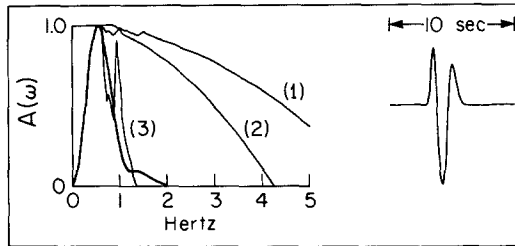$P = 2\pi/L$

L = wavelength of corrugation.

FIG. 13. Theoretical study of the effect free surface topography has on the short-period P wave form. Shown to the *left* are the amplitude spectra of the incident pulse (smooth curve) and three free surface reflection coefficients calculated from the models given in Table 7. Shown at the *right* is the time history of the incident pulse.

TABLE 7

PARAMETER VALUES USED IN REFLECTION COEFFICIENT CALCULATIONS FOR A CORRUGATED FREE SURFACE

Model	α (km/sec)	β (km/sec)	c^* (km)	$L\dagger$ (km)
1	6.0	3.5	0.15	4.0
2	4.0	2.0	0.15	4.0
3	4.0	2.0	0.50	4.0

* c, amplitude of corrugation.

† L, wavelength of corrugation.

Equation (1) applies for small corrugation amplitude, c, relative to the incident wavelength. The use of equation (1) is an approximation inasmuch as the topography will not strictly follow equation (2), and the incident wave is not planar. It should indicate the magnitude of the effect, however, since the teleseismic incident angles are small and the ray parameter (phase velocity) is constant. Figure 13 shows the amplitude spectra of the incident wave and three free surface models given in Table 7. The wavelength and amplitude of corrugation were estimated by consulting topographic maps for the epicentral region (U.S. Department of the Interior, 1960). The values obtained from the topography are given in models (1) and (2), Table 7. Model (3) is considered to be an extreme case. The band of the incident pulse is between 0 and 2 Hz, peaking at about 0.6 Hz and well within the range of applicability for the reflection coefficient. Figure 13 demonstrates that even for the extreme case, model (3), most of the amplitude of the incident wave is unaffected by the corrugation. Synthesis of the resulting short-period wave forms showed no amplitude decrease or distortion, relative to the planar free surface model, for models (1) and (2) and only

a 15 per cent amplitude decrease for model (3). Thus, it is concluded topography does not have a significant effect on the reflection of pP.

The analysis of these far-field data strongly suggest that further constraints on the faulting mechanism of the San Fernando earthquake can be obtained by combining the near-field data. Each taken alone has several obvious uniqueness problems but combined, should help resolve source aspects, especially concerning the initial rupture process. A combined analysis of the far-field A_{LP}/A_{SP} and $A_P/A_P P$ ratios with the Pacoima Dam accelerograms immediately suggests itself to resolve far-field attenuation and characteristics of the initial rupture through a single fault model. For example, the simple propagating line source model used here may not have strict physical meaning for short-period models although its general characteristics are valid in the long-period band. Analysis of rupture models which start at discrete points for differing geometries is probably more physical but is not presently warranted by the teleseismic data. In this respect the short-period models presented here should be taken as preliminary interpretations for the initial faulting process.

The average value of 1.8 km/sec obtained here for rupture velocity is significantly lower than values obtained by others using similar fault geometries (Mikumo, 1973; Boore and Zoback, 1974; Niazi, 1975; McCowan et al., 1977). Using near-field data these authors generally agree to rupture velocities of 2.5 km/sec over much of the fault plane although Boore and Zoback (1974) suggest that rupture slows to less than 2 km/sec near the surface. The value of 1.8 km/sec obtained from the body waves is apparently well constrained largely due to the focal depth. This can be taken as a "maximum" average since lateral fault geometry is well controlled by aftershock locations (Whitcomb et al., 1973) and the epicentral parameters (Allen et al., 1973). In light of the short-period teleseismic results this discrepancy in rupture velocity can be explained by suggesting that the near-field data used by these authors are only a strong function of the initial fault motion near the hypocenter.

The change in fault dip at about 5 km from 53° to 29° is a very interesting structural phenomenon but may be due to a variety of reasons. Whitcomb et al. (1973) discuss several possibilities ranging from similarity with other nearby faults, results from scale model studies (e.g., Sanford, 1959), and the possibility that the San Gabriel fault may form the lower plane (Wesson and Wilson, 1972). This last possibility is intriguing although not preferred by Whitcomb et al. (1973) on the basis of surface geological evidence. Figure 4 does demonstrate an interesting correlation between the breakover point and surface trace of the San Gabriel fault, however. Another possible reason for the change in dip may simply be the change in rock type across the fault. If indeed San Fernando basin sediments are as deep as 5 km, then the inferred breakover point may only be a reflection of this fact.

CONCLUSIONS

Several aspects of the faulting mechanism for the San Fernando earthquake can be resolved by modeling teleseismic P, SH, and SV long- and short-period wave forms using a finite fault representation. Observations of short-period pP fixes the hypocenter at 13 km from an average pP-P time of 4 sec. Modeling the long-period wave forms with the constraints of the locations of the hypocenter and surface breaks yields the fault model listed in Table 5. One of the most important features of this model includes the ability to resolve a change of fault dip during largely unilateral rupture from an initial 53° to about 29° occurring at about 5 km depth. From the timing of this dip change, hypocenter, and shape of long-period P, SH, and SV wave

forms an average rupture velocity of 1.8 km/sec is obtained for the earthquake which is significantly lower than most previous near-field estimates. Short-period pP/P amplitude ratios and long-period/short-period P amplitude ratios strongly suggest that faulting was initially bilateral or possibly unilateral downward with a rupture velocity significantly higher than the average value. This last aspect has important implications for near-field strong-motion modeling since it allows dislocations in the hypocentral region to be reduced by a factor of 2 over simple unilateral upward propagating fault models. It also helps explain previous high estimates of average rupture velocity and the initial sharp shear-wave velocity pulse at Pacoima Dam. Inclusion of the teleseismic body wave data with that of the near field should provide far greater insight into the details of faulting mechanism for the San Fernando earthquake.

APPENDIX I

The following table contains station data for those stations in this study

Code	Location	Δ (°)	Azimuth (°)	Waves Used*
ALE	Alert, Canada	51.8	8.0	$P(+)$, p, SV, $SH(-)$
FBC	Frobisher Bay, Canada	42.2	30.5	$P(+)$, p
FCC	Fort Churchill, Canada	29.2	26.1	$P(+)$
FFC	Flin Flon, Canada	23.3	24.5	$P(+)$
FSJ	Fort Saint James, Canada	20.4	350.2	$P(+)$
MBC	Mould Bay, Canada	41.9	359.7	$P(+)$
MNT	Montreal, Canada	35.7	58.2	$SH(+)$
PNT	Penticton, Canada	14.9	357.0	$P(-)$
SCB	Scarborough, Canada	31.6	61.1	$P(+)$
SCH	Schefferville, Canada	40.9	43.9	p(b)
SFA	Seven Falls, Canada	37.7	55.6	$SH(+)$
STJ	Saint John's, Canada	49.9	53.8	$P(+)$, p(b), SV, $SH(+)$
VIC	Victoria, Canada	14.6	346.7	$P(-)$
YKC	Yellow Knife, Canada	28.2	3.8	$P(+)$
ALQ	Albuquerque, New Mexico	9.9	83.5	$P(+)$
ARE	Arequipa, Peru	67.4	130.6	$P(+)$, p, $SH(+)$
ATL	Atlanta, Georgia	28.2	82.2	p(b)
BEC	Bermuda, Colombia	44.5	76.9	$SH(+)$
BKS	Berkeley, California	4.7	319.3	$P(+)$
BLA	Blacksburg, Virginia	30.8	73.7	$P(+)$, p(b), $SH(+)$
CAR	Caracus, Venezuela	52.5	104.2	$P(+)$, p
COL	College, Alaska	35.3	338.8	$P(+)$, $SH(-)$
COP	Copenhagen, Denmark	81.0	25.7	SV, $SH(+)$
COR	Corvallis, Oregon	10.9	341.1	$P(-)$
DUG	Dugway, Utah	7.3	35.9	$P(-)$
ESK	Eskdalemuir, Scotland	74.9	32.4	p(a)
FLO	Florissant, Missouri	22.9	70.8	$P(+)$
GDH	Godhaven, Greenland	49.4	25.1	SV, $SH(+)$, p(a)
GEO	Georgetown, Washington, D.C.	33.3	70.0	$P(+)$
GIE	Galapagos Islands, Ecuador	43.8	137.1	$P(+)$, p(d)
GOL	Golden, Colorado	11.7	59.3	$P(-)$
HNR	Honiara, Solomon Islands	88.5	257.6	$P(+)$, p

Code	Location	Δ (°)	Azimuth (°)	Waves Used*
JCT	Junction, Texas	16.2	98.8	$P(+)$
KEV	Kevo, Finland	73.1	11.9	$P(+)$, p(a), SV, SH(nodal)
KON	Kongsberg, Norway	77.0	24.2	p(a)
KTG	Kap Tobin, Greenland	60.1	22.7	$P(+)$, p(a), SV, $SH(+)$
LON	Longmire, Washington	12.6	349.2	$P(-)$
LPB	La Paz, Bolivia	69.7	128.1	$P(+)$, $SH(+)$
LPS	La Palma, El Salvador	33.1	120.0	$P(+)$
MAL	Malaga, Spain	86.3	47.4	$P(+)$
MAT	Matsushiro, Japan	79.7	307.2	$P(+)$, p, $SH(-)$
NAT	Natal, Brazil	87.2	98.5	$P(+)$, p
NOR	Nord, Greenland	57.9	9.8	$P(+)$, SV, $SH(-)$
NUR	Nurmijarvi, Finland	80.7	17.5	$P(+)$, p(a), SV
OGD	Ogdensburg, New Jersey	35.0	65.9	p(c)
OXF	Oxford, Mississippi	23.9	81.5	$P(+)$
PEL	Peldehue, Chile	80.7	141.0	$P(+)$, p(d)
PTO	Porto, Portugal	81.0	46.0	$P(+)$, p(b)
QUI	Quito, Ecuador	50.8	124.1	$P(+)$
RCD	Rapid City, S. Dakota	15.2	46.0	$P(-)$
SHA	Spring Hill, Alabama	25.7	89.8	$P(+)$
SJG	San Juan, Puerto Rico	49.1	95.5	$P(+)$, $SH(+)$
STU	Stuttgart, Germany	85.0	31.7	p(a), $SH(+)$
TRI	Trieste, Italy	89.4	31.3	$P(+)$, $SH(+)$
TUC	Tucson, Arizona	6.7	106.0	$P(+)$

* P, long period vertical P wave; p(a), short period vertical P wave, letter in parentheses denotes stacking group of Figure 8; SV, long period radial SV wave; SH, long period tangential SH wave; ($+$ or $-$), polarity of first arrival.

Appendix II

The formulation for the propagating finite line of dislocation was first done by Hirasawa and Stauder (1965). This appendix will present the conventions and coordinates used for the present study in terms of the point source formalism presented by Langston and Helmberger (1975).

Referring to Figure 14, the far-field impulse response for a propagating step function of dislocation on the rectangular fault segment from the origin to $z = b$ is given by

$$I(t, r) = \int\int W(x, z)\delta\left(t - \frac{z}{\xi} - \frac{r}{v}\right) dx\, dz \qquad (A1)$$

where

$$\xi = \text{rupture velocity (also referred elsewhere as } V_R)$$

$$v = \text{wave velocity considered}$$

and in this case the spatial dislocation weighting function

$$W(x, z) = 1.$$

Following the simple developments given by Savage (1966)

$$r = r_0 - \sin\theta\cos(\phi' - \phi)\varrho \qquad (A2)$$

which gives

$$I = \int\int \delta(t + q_1 x - q_2 z) \, dx \, dz \qquad (A3)$$

where

$$\phi' = \text{angle between } z \text{ and } \varrho$$

$$q_1 = \frac{\sin\theta \sin\phi}{v}$$

$$q_2 = \frac{1}{\xi}\frac{\sin\theta \cos\phi}{v} \,.$$
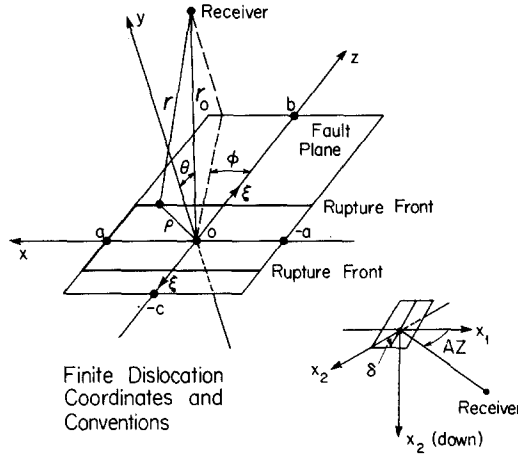

Finite Dislocation
Coordinates and
Conventions

FIG. 14. Coordinates and conventions for the finite dislocation model.

Straightforward integration of (A3) yields

$$I = \frac{1}{q_1 q_2}\{S(t + q_1 a) - S(t - q_1 a) - S(t + q_1 a - q_2 b) + S(t - q_1 a - q_2 b)\} \qquad (A4)$$

where $S(t)$, the ramp function, is the integral of a Heaviside step function. At $\phi = 0$, $n\pi$ or $\theta = 0$ (A3) reduces to

$$I = \frac{2a}{q_2}\{H(t) - H(t - q_2 b)\}. \qquad (A5)$$

For the coordinate system of Langston and Helmberger (1975) (*lower right hand corner* of Figure 14), the ray direction is given by

$$\tan\phi = \frac{\zeta_1}{\zeta_3}$$

$$\sin\theta = (\zeta_1{}^2 + \zeta_3{}^2)^{1/2} \qquad (A6)$$

where

$$\zeta_1 = -\sin \lambda \cos (AZ) \sin i - \cos \lambda \cos \delta \sin AZ \sin i - \epsilon \cos \lambda \sin \delta \cos i$$

$$\zeta_2 = \sin \delta \sin (AZ) \sin i - \epsilon \cos \delta \cos i$$

$$\zeta_3 = \cos \lambda \cos (AZ) \sin i - \sin \lambda \cos \delta \sin (AZ) \sin i - \epsilon \sin \lambda \sin \delta \cos i, \quad \text{(A7)}$$

and where

$$\lambda = \text{rake}$$

$$AZ = \text{station azimuth with respect to fault end}$$

$$\delta = \text{dip}$$

$$i = \text{vertical incident angle}$$

$$\epsilon = \begin{cases} +1, & \text{downgoing ray} \\ -1, & \text{upgoing ray.} \end{cases}$$

The z coordinate is in the rake direction. Spatial coordinates in a layered stack are referenced to the origin of the fault plane. To obtain the solution for the rupturing segment on $z < 0$, b is replaced by c and ϕ with $\phi + \pi$. The resulting time function is then normalized to unit moment in accordance with Langston and Helmberger (1975) by dividing by fault area, or $2a(b + c)$. To include the effect of a propagating ramp dislocation function with rise time, t_R, a simple convolution, denoted by "$*$", of the time derivative of the ramp with I need only be done (Savage, 1966). Explicitly

$$\begin{array}{cc} I & (t) \\ \text{(RAMP)} \end{array} = \begin{array}{cc} I & (t) \\ \text{(STEP)} \end{array} * \frac{H(t) - H(t - t_R)}{t_R} \qquad \text{(A8)}$$

where $H(t)$ is the Heaviside step function.

REFERENCES

Alewine, R. W., III (1974). Application of linear inversion theory toward the estimation of seismic source parameters, *Ph.D. Thesis*, California Institute of Technology, Pasadena, California, 303 pp.

Allen, C. R., T. C. Hanks, and J. H. Whitcomb (1973). San Fernando earthquake: Seismological studies and their implications, in *San Fernando, California, Earthquake of February 9, 1971, Volume I, Geological and Geophysical Studies*, U.S. Government Printing Office, Washington, D.C.

Anderson, D. L., A. Ben Menahem, and C. B. Archambeau (1965). Attenuation of seismic energy in the upper mantle, *J. Geophys. Res.* **70**, 1441–1448.

Barrows, A. G., J. E. Kahle, F. H. Weber, Jr., and R. B. Saul (1973). Map of surface breaks resulting from the San Fernando, California earthquake of February 9, 1971, in *San Fernando, California, Earthquake of February 9, 1971, Volume III, Geological and Geophysical Studies*, U.S. Government Printing Office, Washington, D.C.

Boore, D. M. and M. D. Zoback (1974). Two-dimensional kinematic fault modeling of the Pacoima

Dam strong-motion recordings of the February 9, 1971, San Fernando earthquake, *Bull. Seism. Soc. Am.* **64**, 555–570.

Burdick, L. J. (1977). Broad-band seismic studies of body waves, *Ph.D. Thesis*, California Institute of Technology, Pasadena, California.

Burdick, L. J. and C. A. Langston (1977). Modeling crustal structure through the use of converted phases in teleseismic body-wave forms, *Bull. Seism. Soc. Am.* **67**, 677–691.

Canitez, N. and M. N. Toksoz (1972). Static and dynamic study of earthquake source mechanism: San Fernando earthquake, *J. Geophys. Res.* **77**, 2582–2594.

Carpenter, E. W. (1966). Absorption of elastic waves—an operator for a constant Q mechanism, *Atomic Weapons Res. Estab. Rep. 0-4366*, Her Majesty's Sta. Office, London.

Dillinger, W. H. (1973). Focal mechanism of San Fernando earthquake, in *San Fernando, California Earthquake of February 9, 1971, Volume III, Geological and Geophysical Studies*, U.S. Government Printing Office, Washington, D.C.

Duke, C. M., J. A. Johnson, Y. Kharraz, K. W. Campbell, and N. A. Malpiede, (1973). Subsurface site conditions in the San Fernando earthquake area, in *San Fernando, California Earthquake of February 9, 1971, Volume IB, Buildings-Soils and Foundations*, U.S. Government Printing Office, Washington, D.C.

Farnbach, J. S. (1975). The complex envelope in seismic signal analysis, *Bull. Seism. Soc. Am.* **65**, 951–962.

Fuchs, K. (1966). The transfer function for P waves for a system consisting of a point source in a layered medium, *Bull. Seism. Soc. Am.* **56**, 75–108.

Fukao, Y. (1971). Seismic body waves from surface faults, *J. Phys. Earth (Tokyo)* **19**, 271–281.

Futterman, W. I. (1962). Dispersive body waves, *J. Geophys. Res.* **67**, 5279–5291.

Gilbert, F. (1964). Propagation of transient leaking modes in a stratified elastic waveguide, *Rev. Geophys.* **2**, 123–153.

Hagiwara, T. (1958). A note on the theory of the electromagnetic seismograph, *Bull. Earthquake Res. Inst., Tokyo Univ.* **36**, 139–164.

Hanks, T. C. (1974). The faulting mechanism of the San Fernando earthquake, *J. Geophys. Res.* **79**, 1215–1229.

Harkrider, D. G. (1964). Surface waves in multilayered elastic media, I. Rayleigh and Love waves from buried sources in a multilayered elastic half-space, *Bull. Seism. Soc. Am.* **54**, 627–679.

Hart, R. S., R. Butler, and H. Kanamori (1977). Surface-wave constraints on the August 1, 1975, Oroville earthquake, *Bull. Seism. Soc. Am.* **67**, 1–7.

Haskell, N. A. (1953). The dispersion of surface waves on multilayered media, *Bull. Seism. Soc. Am.*, **43**, 17–34.

Helmberger, D. V. (1974). Generalized ray theory for shear dislocation, *Bull. Seism. Soc. Am.* **64**, 45–64.

Helmberger, D. V. and G. R. Engen (1974). Upper mantle shear structure, *J. Geophys. Res.* **79**, 4017–4028.

Herrmann, R. B. (1976). Some more complexity in S-wave particle motion, *Bull. Seism. Soc. Am.* **66**, 625–632.

Hileman, J. A., C. R. Allen, and J. M. Nordquist (1975). *Seismicity of the Southern California Region 1 January 1932 to 31 December 1972*, Seismological Laboratory, California Institute of Technology, Pasadena, California.

Hirasawa, T. and W. Stauder, S. J. (1965). On the seismic body waves from a finite moving source, *Bull. Seism. Soc. Am.* **55**, 237–262.

Johnson, J. A. and C. M. Duke (1973). Subsurface geology of portions of San Fernando Valley and Los Angeles basin, in *San Fernando, California Earthquake of February 9, 1971, Volume III, Geological and Geophysical Studies*, U.S. Government Printing Office, Washington, D.C.

Jungels, P. H. and G. A. Frazier (1973). Finite element analysis of the residual displacements for an earthquake rupture: Source parameters for the San Fernando earthquake, *J. Geophys. Res.* **78**, 5062–5083.

Kanamori, H. and D. Hadley (1975). Crustal structure and temporal velocity change in Southern California, *Pageoph.* **113**, 257–280.

Langston, C. A. (1975). The relationship between the teleseismic P-wave and near-field strong motion observations for the February 9, 1971 San Fernando earthquake (abstract), *Earthquake Notes* **46**, 39.

Langston, C. A. (1976a). A body wave inversion of the Koyna, India earthquake of December 10, 1967, and some implications for body wave focal mechanisms, *J. Geophys. Res.* **81**, 2517–2529.

Langston, C. A. (1976b). Body wave synthesis for shallow earthquake sources: Inversion for source and earth structure parameters, *Ph.D. Thesis*, California Institute of Technology, Pasadena, California, 214 pp.

Langston, C. A. (1977). The effect of planar dipping structure on source and receiver responses for constant ray parameter, *Bull. Seism. Soc. Am.* 67, 1029–1050.

Langston, C. A. and D. V. Helmberger (1975). A procedure for modeling shallow dislocation sources, *Geophys. J.* 42, 117–130.

Langston, C. A. and R. Butler (1976). Focal mechanism of the August 1, 1975 Oroville earthquake, *Bull. Seism. Soc. Am.* 66, 1111–1120.

Langston, C. A. and D. E. Blum (1977). The April 29, 1965 Puget Sound earthquake and the crustal and upper mantle structure of western Washington, *Bull. Seism. Soc. Am.* 67, 693–711.

McCowan, D. W., P. Glover, and S. S. Alexander (1977). A static and dynamic finite element analysis of the 1971 San Fernando, California earthquake, *Geophys. J.* 48, 163–185.

Mellman, G., L. Burdick, and D. Helmberger (1975). Determination of source parameters from body wave seismograms (abstract), *Earthquake Notes* 46, 44.

Mitchell, B. J. and M. Landisman (1969). Electromagnetic seismograph constants by least-squares inversion, *Bull. Seism. Soc. Am.* 59, 1335–1348.

Mikumo, T. (1969). Long-period P waveforms and the source mechanism of intermediate earthquakes, *J. Phys. Earth (Tokyo)* 17, 169–313.

Mikumo, T. (1973). Faulting process of the San Fernando earthquake of February 9, 1971 inferred from static and dynamic near-field displacements, *Bull. Seism. Soc. Am.* 63, 249–269.

Niazi, A. (1975). An exact solution for a finite, two-dimensional moving dislocation in an elastic half-space with application to the San Fernando earthquake of 1971, *Bull. Seism. Soc. Am.* 65, 1797–1826.

Oliver, J. (1961). On the long period character of shear waves, *Bull. Seism. Soc. Am.* 51, 1–12.

Sanford, A. R. (1959). Analytical and experimental study of simple geologic structures, *Bull. Geol. Soc. Am.* 70, 19–52.

Sato, R. (1955). The reflection of elastic waves on corrugated surface, *Zisin* (ii), 8, 8–22.

Savage, J. C. (1966). Radiation from a realistic model of faulting, *Bull. Seism. Soc. Am.* 56, 577–592.

Su, S. S. and J. Dorman (1965). The use of leaking modes in seismogram interpretation and in studies of crust-mantle structure, *Bull. Seism. Soc. Am.* 55, 989–1021.

Thatcher, W. (1976). Episodic strain accumulation in Southern California, *Science* 194, 691–695.

Trifunac, M. D. (1974). A three-dimensional dislocation model for the San Fernando, California earthquake of February 9, 1971, *Bull. Seism. Soc. Am.* 64, 149–172.

Trifunac, M. D. and D. E. Hudson (1971). Analysis of the Pacoima Dam accelerogram—San Fernando, California earthquake of 1971, *Bull. Seism. Soc. Am.* 61, 1393–1411.

U.S. Department of the Interior, Geological Survey (1960). Mint Canyon 7.5′ Quadrangle, State of California, Department of Water Resources.

Wesson, R. L. and D. H. Wilson (1972). Faulting in the San Fernando earthquake of February 9, 1971 (abstract), *Trans. Am. Geophys. Union* 53, 449.

Whitcomb, J. H., C. R. Allen, J. D. Garmany, and J. A. Hileman (1973). San Fernando earthquake series, 1971: Focal mechanisms and tectonics, *Rev. Geophys. Space Phys.* 11, 693–730.

Wyss, M. and T. C. Hanks (1972). The source parameters of the San Fernando earthquake inferred from teleseismic body waves, *Bull. Seism. Soc. Am.*, 62, 591–602.

DIVISION OF GEOLOGICAL AND PLANETARY SCIENCES
CALIFORNIA ITSTITUTE OF TECHNOLOGY
PASADENA, CALIFORNIA 91125
CONTRIBUTION No. 2946